International Journal of Technology 14(3) 669-679 (2023)
Received October 2021 / Revised November 2021 / Accepted March 2022

International Journal of Technology

A Novel Lanthanum-based Solid Oxide Fuel Cell Electrolyte Composite with Enhanced Thermochemical Stability toward Perovskite Cathode

Atiek Rostika Noviyanti[1*], Yoga Trianzar Malik[1], Uji Pratomo[1], Dani Gustaman Syarif[2]

[1]*Department of Chemistry, Faculty of Mathematics and Sciences, Universitas Padjadjaran, Jl. Raya Bandung-Sumedang KM. 21, Jatinangor 45363, Indonesia*
[2]*PRTNT-ORTN-BRIN, Jl. Taman Sari 71, Bandung 40132, Indonesia*

Abstract. Lanthanum-based electrolytes for Solid Oxide Fuel Cells (SOFCs) gain extensive attention due to their lower activation energy and low-cost preparation to convert the energy stored in gaseous chemicals into electricity. In this context, a $La_{9.33}Si_6O_{26}$-$La_{0.8}Sr_{0.2}Ga_{0.8}Mg_{0.2}O_{2.55}$ (LSO-LSGM) SOFC electrolyte composite with various mass ratio LSO:LSGM (w/w) (5:0, 4:1, 3:2, 2:2, 2:3, 1:4) are successfully prepared for the first time using different LSO precursors with various mass target of 3g (LSO-$LSGM_A$) and 5g (LSO-$LSGM_B$), respectively. The result shows that the lower mass target in the synthesis of LSO induced formation of protoenstatite and coesite secondary phases on the composite of LSO-LSGM based on XRD, FTIR, and XPS analysis. The SEM micrograph suggests that agglomeration occurred more in LSO-$LSGM_A$ than in LSO-$LSGM_B$. Generally, the composites signified high chemical stability on $La_{0.8}Sr_{0.2}Co_{0.6}Fe_{0.4}O_{2.55}$ (LSCF) cathode based on the XRD analysis. The LSO-$LSGM_A$ composites which contained a high percentage of protoenstatite and coesite resulted in an additional peak of $MgSi_2Sr$, especially for the sample with the mass ratio of 41 (LSO-LSGM41) suggesting that the chemical stability of LSO-$LSGM_A$ on LSCF cathode is much lower than LSO-$LSGM_B$.

Keywords: LSCF cathode; LSO-LSGM; Solid oxide fuel cell; Solid state method

1. Introduction

The Solid Oxide Fuel Cell (SOFC) is a device that can generate electricity from gaseous chemicals (hydrogen or short-chained hydrocarbon). It operates at high temperatures up to 1400K (Abdalla *et al.*, 2018). Similar to the fuel cell (Mulyazmi *et al.*, 2019), the electrolyte in SOFC portrays an important role in a set of operating temperatures and thermochemical stability at high temperatures. Yttrium-stabilized zirconia (YSZ) with general formula $(ZrO_2)_{1-x}$ $(Y_2O_3)_x$ and $0.08 \leq x \leq 0.1$ can generate ionic conductivity for oxide ion up to 2.00×10^{-1} $S.cm^{-1}$ (1273K) for an ideal condition (Rahmawati *et al.*, 2017; Preux, Rolle, and Vannier, 2012). However, a lower temperature can drop the conductivity to 1.02×10^{-3} $S.cm^{-1}$ (973K) (Rajesh and Singh, 2014) due to high activation energy (*E*a) varied from 0.89 to 1.16 eV (Zarkov *et al.*, 2015), and another study noted the value as 1.21 eV (Rajesh and Singh, 2014). YSZ electrolyte is also reported unavailable to sustain chemical stability with

*Corresponding author's email: atiek.noviyanti@unpad.ac.id, Tel.: +6222-7794391; Fax.: +62227794391
doi: 10.14716/ijtech.v14i3.5189

perovskite electrodes such as LSCF and LSM cathode at 1300 K (Fan, Yan, and Yan, 2011; Minh and Takahashi, 1995).

Lanthanum silicate oxides (LSO) electrolyte with the formula of $La_{10-x}(SiO_4)_6O_{2-d}$, x=0.1-0.6 has a potential characteristic to substitute YSZ conventional electrolyte. LSO is more stable than YSZ at high temperatures in the case with no reactivity to perovskite cathode at 1300 K (Marrero-López, *et al*., 2010). Moreover, the *E*a of LSO is much lower than YSZ (up to 32 eV) (Kim *et al*., 2011) despite the ionic conductivity that is required to be improved. The ionic conductivity of LSO varied from 1.58×10^{-2} to 3.16×10^{-1} S.cm^{-1} (1273 K) (Higuchi *et al*., 2010). The structure of LSO is made of an isolated unit of SiO_4 tetrahedral which creates disparate channels parallel to the c-axis. The smaller of these channels contains lanthanum cations and vacancies, while the larger one contains both lanthanum cations and oxide ions which are responsible for the ionic conduction channel (Masson *et al.,* 2017). The lanthanum ions are coordinated with this isolated tetrahedral SiO_4 which can form a hexagonal structure with $P\bar{3}$, $P6_3$, or either $P6_3$ space group which can be doped with other elements such as bismuth (Noviyanti *et al.,* 2021).

The composite strategy is one of the best methods to manage this issue due to its ability to signify a better result in lowering *E*a rather than the doping method. The composite method also can overcome a reduction issue in some SOFC electrolytes that may lead to lowering electrical performance (Raza *et al*., 2020). LSO-YSZ (Noviyanti *et al*., 2016), LSO-CGO (Noviyanti *et al*., 2018), and LSGM-YSZ (Raghvendhra *et al*., 2014) denoted a decrease of *E*a as the addition of the composites, while the addition of Sr-doping to La site in LSO phase increases the value of *E*a two times larger, from 0.56 eV to 1.26 eV (Leon-Reina *et al*., 2004). LSGM electrolyte was chosen with LSO for the composite due to the high ionic conductivity (5.62×10^{-1} S.cm^{-1} at 1273 K) and a thermal expansion coefficient (TEC) of 12.7×10^{-6} K^{-1} (Kharton, Marques, and Atkinson, 2004), and lower *E*a than YSZ (0.82 eV) (Huang, and Goodenough, 2000). With this combination of LSO-LSGM, it is expected to result in excellent performance and high thermochemical stability on the LSCF cathode. Thermochemical stability is quite important to enhance the electrochemical performance of SOFC cells during high operating temperatures. The low thermochemical stability will lead to cell degradation and the short life of SOFC energy generation. However, to obtain a high-stable electrolyte composite on a typical perovskite SOFC cathode at high operating temperature, any impurities from constituents of the composite should be reduced. From all the aforementioned studies, the impurity effect was not comprehensively studied. Thus, an attempt to design a novel composite of LSO-LSGM and a thorough study of impurities effect in LSO-LSGM composite on thermochemical stability of LSO-LSGM on LSCF cathode was carried out to understand the origin of enhanced thermochemical stability of LSO-LSGM composite.

To our knowledge, the detailed preparation of LSO-LSGM with various mass ratios of LSO and LSGM and its chemical stability test on the LSCF cathode has not been reported yet. Our study found that the different mass targets during the synthesis of LSO can implicitly induce a formation of protoenstatite and coesite phase in LSO-LSGM which can increase the formation of $LaSrGaO_4$ in the LSO-LSGM/LSCF interface. This study aims to prepare the composites of LSO-LSGM and examines the chemical stability of LSO-LSGM on the LSCF perovskite cathode. The LSO precursor was synthesized using the hydrothermal method accorded with our previous study. In addition, the investigation of the effect of $La(OH)_3$ impurities amount that was found in LSO synthesis on the phase formation in LSO-LSGM composites and chemical stability on the LSCF perovskite cathode was carried out.

2. Methods

2.1. LSO-LSGM preparation

The LSO-LSGM composites were prepared using the conventional solid-state method (Malik *et al.*, 2018). Generally, the synthesized LSO and commercially-available LSGM were mixed with the different mass ratios in ethanol using *Agate* mortar. The mixture was subsequently dried in the oven at 393K for 2h. The mixture powder was pelleted with a circular diameter of 15 mm. The pellet of LSO-LSGM was sintered in a furnace at 1473K for 8h as illustrated in Figure 1. LSOs with 3 and 5 g mass targets were synthesized using the hydrothermal method as provided in our previous study (Malik *et al.*, 2019). LSGM and LSCF were obtained from Sigma (99.99%, metal basis trace). The composites were divided into two categories: A (using LSO precursors with 3 g mass target) with various mass ratios of LSO:LSGM (w/w) = 5:0 (LSO_A), 4:1 (LSO-$LSGM_A$41), 3:2 (LSO-$LSGM_A$32), 2:2 (LSO-$LSGM_A$22), 2:3 (LSO-$LSGM_A$23), 1:4 (LSO-$LSGM_A$14), 5:0 (LSGM) and B (using LSO precursor with 5 g mass target) with various mass ratio of LSO:LSGM (w/w) = 5:0 (LSO_B), 4:1 (LSO-$LSGM_B$41), 3:2 (LSO-$LSGM_B$32), 2:2 (LSO-$LSGM_B$22), 2:3 (LSO-$LSGM_B$23), 1:4 (LSO-$LSGM_B$14), 5:0 (LSGM). LSO-LSGM composites were characterized using XRD (D8 Bruker Advanced) at 2θ range of 10–70° with Cu Kα radiation, λ = 0.15418 nm and v = 0.02° min^{-1} to examine the crystal structures, Fourier transformation infrared/FTIR (Fischer Scientific) to study the chemical bonding, X-ray photoelectron spectroscopy/XPS (JEOL JPS-9010MX) to examine the chemical state of the composition elements, and SEM (JEOL JSM-7500f) with 10000× magnification to analyze the microstructure of LSO-LSGM composite electrolytes.

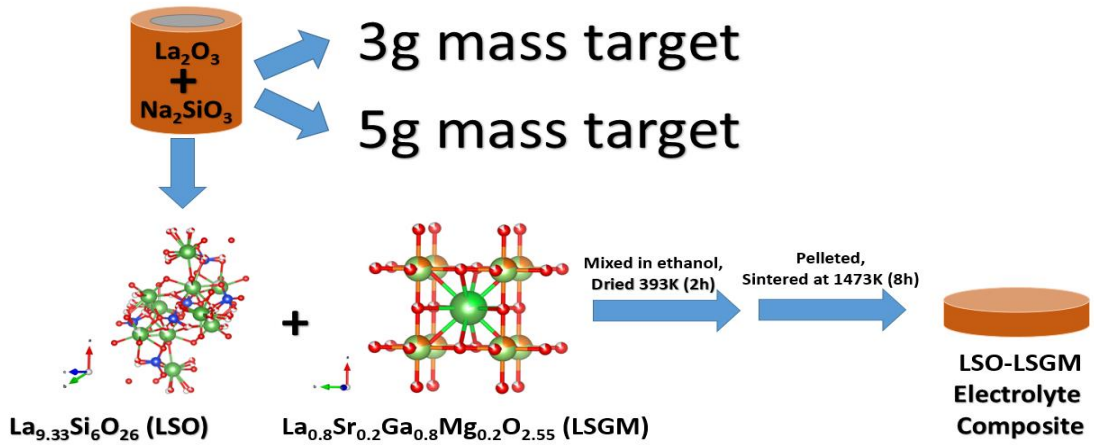

Figure 1 Schematic illustration of LSO-LSGM electrolyte composite preparation

2.2. Thermochemical stability analysis

Thermochemical stability was assessed based on the level of LSO-LSGM electrolyte reactivity to the LSCF cathode. LSO-LSGM electrolytes are mixed with LSCF cathode using ball milling for 2 hours with a mass ratio (w/w) LSO: LSGM of 1:1. This mixture is heated in a furnace for 48 hours at a temperature of 1473 K. The heating mixture was characterized using XRD Bruker D8 Advanced, Cu Kα radiation, λ = 0.15418 nm, T = 298 K, v = 0.02° min^{-1} in the range of 10-70°. The results of the XRD pattern are analyzed to observe the possibility of new crystalline phases emanating from the electrolyte-electrode interactions. The XRD patterns were refined using *Highscoreplus*© (Degen *et al.*, 2014).

3. Results and Discussion

3.1. Characterization of Novel LSO-LSGM Electrolyte Composites

The prepared LSO-LSGM composite was characterized using XRD and FTIR. The results suggested that the formation of LSO-LSGM was successful. The detail of each characterization is discussed below.

3.1.1. XRD Characterization

The LSO-LSGM electrolyte composites were successfully prepared using the solid phase synthesis method. The XRD diffraction patterns varied from each LSO-LSGM composition (as shown in Figure S1). The main peak intensity of LSGM diffraction at 2θ = 33° decreases along with increasing LSO composition in LSO-LSGM composites which are characterized by strengthening intensities of LSO peak diffraction. Based on this XRD pattern, the composting process ran according to our expectations, where both the LSO and LSGM peaks are found in each LSO-LSGM diffraction composite pattern, in all LSO-LSGM various mass ratios.

The LSGM deployed in this study has a cubic-based structure with a P *m-3m* space group that correlates with $La_{0.8}Sr_{0.2}Ga_{0.8}Mg_{0.2}O_{2.55}$ ($LSGM_{0802}$) ICSD No. standard phase. 98-009-8170. The structure of LSGM with this composition can be maintained in a mixed phase of the LSO-$LSGM_A32$, LSO-$LSGM_A22$, LSO-$LSGM_A23$, LSO-$LSGM_A14$, and LSO-$LSGM_B32$, LSO-$LSGM_B22$, LSO-$LSGM_B23$, LSO-$LSGM_B14$. Meanwhile, for the LSO-$LSGM_A41$ and LSO-$LSGM_B41$ composite electrolytes, the LSGM constituent was compatible with the LSGM phase of $La_{0.9}Sr_{0.1}Ga_{0.8}Mg_{0.2}O_{2.55}$ ($LSGM_{0901}$).

The XRD pattern, shown in Figure 2, informs that the LSO yielded a secondary phase with LSGM known as protoenstatite ($MgSiO_3$) and coesite (SiO_2) in both categories of LSO-$LSGM_A32$, LSO-$LSGM_A22$, LSO-$LSGM_A23$ and LSO-$LSGM_B32$, LSO-$LSGM_B22$, LSO-$LSGM_B23$. The main peak of protoenstatite was signified at 27.67°, while the peak of the diffraction phase of the coesite was indicated at 29.28°.

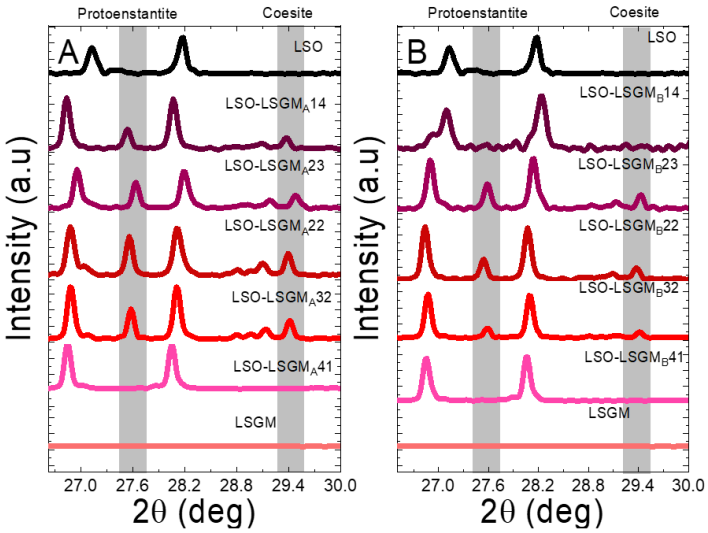

Figure 2 XRD pattern of LSO-$LSGM_A$ (left) and LSO-$LSGM_B$ (right) composite electrolytes at the range of 2θ = 25−30°. The coesite phase is indicated at 2θ of 27.67° and protoenstantite phase

As shown in Figure 3, the LSO-LSGM 41 and 14 composites in both categories show a peak phase of $LaGaSrO_4$, which is a common secondary phase that is often found in LSGM-based composites. This phenomenon indicates that the $LaGaSrO_4$ phase can be formed in composites with a low precursor composition concentration of LSGM and LSO. Moreover,

the composition of the $LaGaSrO_4$ phase in the LSO-$LSGM_A$ composite is known to be higher than in the LSO-$LSGM_B$ composite which indicates that the target mass of 5g could be better than LSO with a target mass of 3g as a precursor of LSO composites. Moreover, the formation of coesite (SiO_2) may closely relate to the preparatory stage of LSO-LSGM electrolyte composite using the solid-phase method at 1273K (Mart *et al.*, 2008). Meanwhile, the presence of hydroxide (−OH) species from $La(OH)_3$ impurities in the LSO precursors contribute to the formation of the protoenstatite ($MgSiO_3$) phase in LSO-LSGM. This behavior is in line with research by Karakchiev *et al.* (2009), which explains that a protoenstatite phase can be formed if species such as Mg^{2+}, OH^-, and SiO_2 are introduced in the system.

The percentage of impurity phases in the LSO-LSGM electrolyte composite is shown in Table 1. The level of impurities in LSO-$LSGM_B$ was much less than that of LSO-$LSGM_A$ electrolytes. This behavior indicates that the impurity of $La(OH)_3$ from LSO is assumed to influence the formation of the two phases. Composites prepared from LSO with lower levels of impurities tend to reduce the level of impurities on the composite electrolytes. Thus, the LSO-$LSGM_B$ composite electrolyte can be said to have better characteristics compared to the LSO-$LSGM_A$.

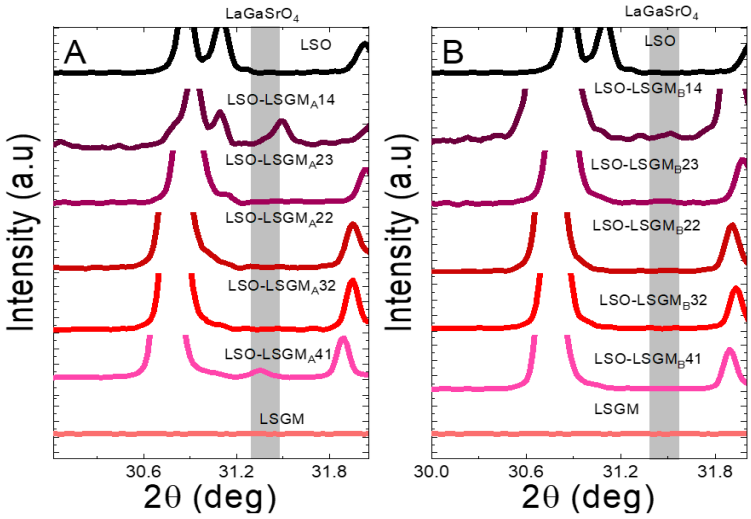

Figure 3 XRD pattern of LSO-$LSGM_A$ (left) and LSO-$LSGM_B$ (right) composite electrolytes at the range of 2θ = 30−33°. $LaGaSrO_4$ phase is indicated at 2θ of ~31.5 in LSO-LSGM41 and LSO-LSGM14, respectively.

Table 1 Percentage of impurity phase in LSO-$LSGM_A$32, LSO-$LSGM_A$22, and LSO-$LSGM_A$23 electrolyte composites.

LSO-$LSGM_A$	Coesite/ %	Protoenstatite/ %	LSO-$LSGM_B$	Coesite/ %	Protoenstatite/ %
32	16.8	17.5	32	8.3	9.8
22	14.2	16.8	22	7.6	12.5
23	6.5	13.5	23	5.4	11.3

The composite electrolyte lattice parameter of LSO-LSGM is shown in Table 2. As shown in Table 2, the LSO phase of the LSO-LSGM composite has a larger volume of crystal cell units than the standard LSO (589.26 $Å^3$). Meanwhile, the LSGM phase tends to have a fixed volume with the standard LSGM (60.01 $Å^3$) except for LSO-$LSGM_A$41. This result confirmed that the LSO-$LSGM_A$41 correlated to $LSGM_{0901}$ more than to $LSGM_{0802}$. The presence of $La(OH)_3$ impurities from high LSO precursors in this composition is thought to affect the volume expansion behavior of the cell unit of the composite electrolyte.

Another behavior that can be observed from the changes in the volume of LSO-LSGM electrolyte composite cell units is that it induced an increase in LSGM cell unit volume which consistently occurred in LSO-LSGM32, LSO-LSGM22, LSO-LSGM23 (both composite categories) accordingly with the decrease in LSO cell unit volume (Figure S2). This behavior is closely related to the discovery of the same type of impurity phase.

Table 2 LSO-LSGM$_A$ and LSO-LSGM$_B$ composite electrolyte lattice parameters

Category A (LSO-LSGM$_A$)

Lattice Parameters					
	LSO$_A$			LSGM	
LSO-LSGM	a=b/ Å	c/ Å	V/ Å^3	a=b=c / Å	V/ Å^3
41	9.7494(8)	7.2531(8)	597.08	3.9829(9)	63.19
32	9.7434(6)	7.2555(0)	596.53	3.9151(9)	60.01
22	9.7372(0)	7.2527(2)	595.54	3.9154(9)	60.03
23	9.7380(7)	7.2537(0)	595.72	3.9158(3)	60.04
14	9.6983(4)	7.1922(4)	585.87	3.9131(8)	59.92

Category B (LSO-LSGM$_B$)

Lattice Parameters					
	LSO$_B$			LSGM	
LSO-LSGM	a=b/ Å	c/ Å	V/ Å^3	a/ Å	V/ Å^3
41	9.7465(3)	7.2517(3)	596.60	3.9171(7)	60.11
32	9.7435(8)	7.2552(3)	596.52	3.9131(1)	59.92
22	9.7400(5)	7.2538(5)	595.98	3.9139(7)	59.96
23	9.7365(1)	7.2536(9)	595.53	3.9148(4)	60.00
14	9.7198(2)	7.2411(0)	592.46	3.9133(0)	59.93

3.1.2. FTIR Analysis

To confirm the occurrence of the impurity phases of protoenstantite and coesite and to investigate the bond interaction in the LSO-LSGM composite, FTIR analysis was also carried out (see Figure 4). The occurrence of these impurities may affect the chemical stability of LSO-LSGM with the LSCF cathode. LSO has the main band at a wave number of 915−980 cm^{-1} which shows the SiO_4 asymmetric stretch vibration, while LSGM shows the stretch of Ga-O bonds band at 635 cm^{-1}, La-Mg bonds at 1470 cm^{-1}, and Mg-O bonds at 3368 cm^{-1} (Byszewski *et al*., 2006; Baran, 1975). The increasing LSGM mass in the LSO-LSGM composite affected band changes at 635cm^{-1} which corresponds to the number of Ga-O bonds. The vibration band for the -OH bond (3600 cm^{-1}) that was found in LSO, does not appear at the LSO-LSGM composite. On the other hand, there is an occurrence of the band from the Mg-O bond shown at 3368 cm^{-1}.

The LSO-LSGM$_A$ showed a different peak from LSO-LSGM$_B$ at 2800 cm^{-1}, which corresponds to the stretch vibration of Mg−Si of protoenstatite phases. The Si-O-Si bonds from LSO$_A$ considerably have contributed to an increasing intensity of wave number 1500 cm^{-1} due to Mg−Si bonds in the $MgSiO_3$ enstatite phase can occur at 1509 cm^{-1} (Kalinkina *et al*., 2001).

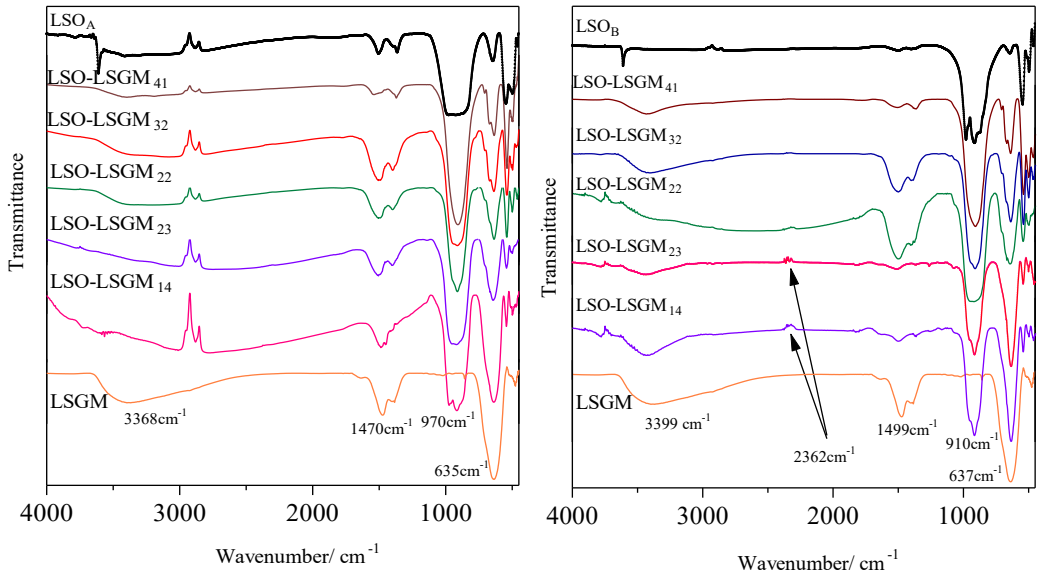

Figure 4 FTIR spectrum of LSO-LSGM prepared from LSO_A (left) and LSO_B (right).

3.2. Fourier Map Analysis of LSO-LSGM

The Fourier map analysis was carried out to observe changes in electron density in the ionic conduction pathway. The result of the Fourier map is shown in Figure S3 and Figure S4. The green color represents the high electron density level (positive) in the LSO phase which becomes more concentrated as the level of LSGM increases. Meanwhile, the color blue or red represents negative density or low electron density (Masson *et al.*, 2017; Galindo-hernández, and Gómez, 2009).

The different levels of electron density reinforce the notion that variations in target mass synthesis can affect the fundamental characteristics of the LSO-LSGM electrolyte composites. Composite electrolytes containing LSO with higher impurity levels have lower electron density compared to composite electrolytes prepared from LSO precursors with lower impurity levels.

3.3. Surface characterization of LSO-LSGM by Scanning Electron Microscopy (SEM)

The micrograph SEM (as seen in Figure 5) was conducted to study the surface and grain morphology of LSO-LSGM and to examine microstructure differences between LSO-$LSGM_A$ and LSO-$LSGM_B$ powders. The micrographs suggested a disparate microstructure of the electrolytes at which the agglomeration of LSO-$LSGM_A$ micro-grains more pronouncedly observed comparing to the LSO-$LSGM_B$, especially for LSO-$LSGM_A$32, LSO-$LSGM_A$22, and LSO-$LSGM_A$23. The grains form a nearly uniform rectangle-to-hexagonal-like shape which resembles the hexagonal and cubic-based structure according to XRD analysis.

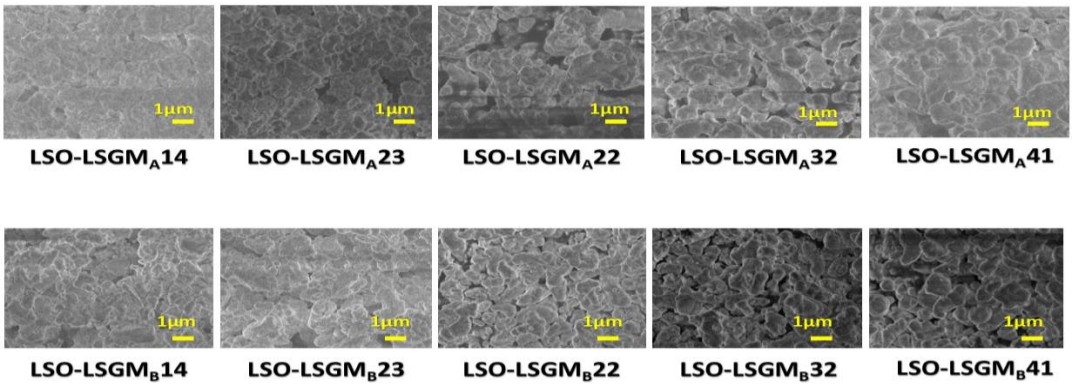

Figure 5 SEM micrographs of LSO-$LSGM_A$ and LSO-$LSGM_B$ (10.000× magnification)

3.4. X-ray photoelectron spectroscopy (XPS) of LSO-LSGM

X-Ray photoelectron spectroscopy was employed to examine the chemical state of the composition elements and the surface properties of LSO-LSGM$_A$ and LSO-LSGM$_B$. The XPS spectrum is shown in Figure S5. The C1*s* spectrum displays a characteristic shoulder due to carbonates at a binding energy (BE) of 289.5 eV. The strong peak at BE 285.0 eV indicates the presence of amorphous carbon on the surface. The BE peaks of La 3d, Sr 3d, Ga 2p, and O1s have been observed at 836, 135, 1117, and 530 eV, respectively, which is similar to Raghvendhra *et al.* (2014). However, Si 2s spectra were not observed at 152 eV for LSO-LSGM$_A$. It may be due to an overlap with the Ga 3s spectrum that emerged at 153 eV (Kharlamova, 2014).

3.5. Thermochemical stability test of LSO-LSGM

To investigate the thermochemical stability of LSO-LSGM towards a typical LSCF perovskite cathode, a thermal test was performed. As prepared LSO-LSGM was mixed equally with the LSCF cathode and heated at a high temperature of 1473 K for 48h. Thermochemical stability refers to the ability of the LSO-LSGM electrolyte composite to maintain its phase when reacted with the LSCF cathode. The chemical reactions that do not occur between the LSO-LSGM and LSCF phases indicate good thermochemical stability, in this case: LSO-LSGM towards LSCF. This chemical reactivity can be observed through the formation of other phases which are by-products of the LSO, LSGM, and LSCF components. The formation of these by-products is marked by the appearance of new peaks on the XRD pattern (Figure 6 and Figure S6. The LSCF perovskite cathode depicted typical peaks at 2θ of 23°, 32.5°, and 40° (Figure S6) which was consistently found in other studies (Adi, Manaf, and Ridwan, 2017). These peaks, moreover, remained the same even after being combined with LSO-LSGM electrolyte composite, except for the emergence of a new peak at ~27.6°, which was furthermore indicated as a discussed protoenstantite phase below.

The LSO-LSGM$_B$ composites with all the LSO to LSGM ratios showed relatively lower reactivity toward the LSCF cathode compared to LSO-LSGM$_A$ as expected (as shown in Figure 5a and Figure 5b). Surprisingly, the protoenstantite phase which priory found at 2θ of 27.67° noticeably disappeared at LSO-LSGM$_B$32, LSO-LSGM$_B$22, and LSO-LSGM$_B$22, respectively. The result indicates that the higher mass target during LSO synthesis can lead to the lower reactivity of the LSO-LSGM composite toward the LSCF cathode. The ratio of protoenstantite phase in all LSO-LSGM$_B$ is much lower than in LSO-LSGM$_A$ (shown in Figure 5c). Hence, the LSO electrolytes with lower impurity levels can increase the chemical stability of the LSCF cathode in LSO-LSGM composite electrolytes and the chemical stability of the LSO-LSGM electrolyte can be controlled through the LSO precursor.

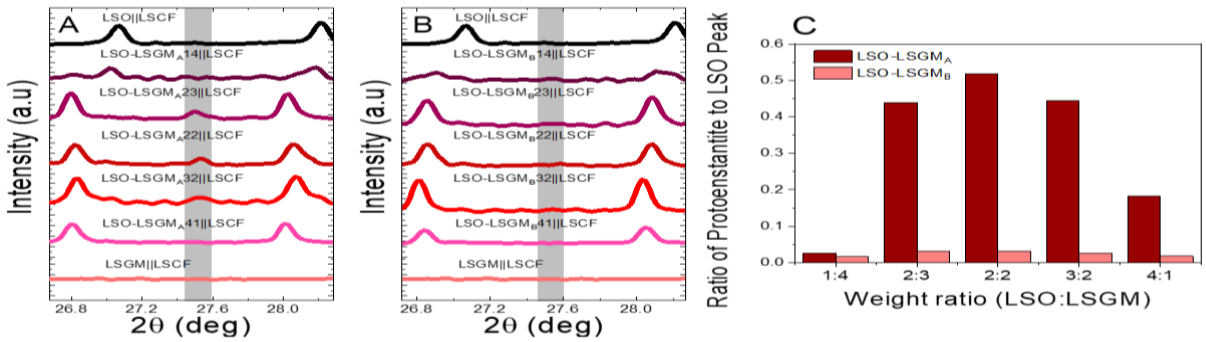

Figure 6 XRD pattern of LSO-LSGM$_A$ (A), LSO-LSGM$_B$ (B) composite electrolytes at the range of 2θ = 27–30°, and (C) Peak ratio of protoenstantite phase to a neighbour peak of LSO at 2θ of 28°

4. Conclusions

The LSO-LSGM composite has been successfully prepared. The XRD pattern suggested that LSO-LSGM$_B$ has higher thermochemical stability compared to LSO-LSGM$_A$. This higher stability originated from the different phase impurities in the LSO precursor which lead to the formation of protoenstantite and coesite phases in LSO-LSGM composites. The phases of protoenstatite and coesite appeared in the LSO-LSGM with the range of mass ratio (LSO to LSGM) of 3:2 to 2:3. The LSO-LSGM$_A$ contained more coesite of 6.5 to 16.8% and protoenstatite of 13.5 to 17.5% compared to the LSO-LSGM$_B$ which showed the coesite phase of 5.4 to 8.3% and protoenstatite of 9.8 to 11.3%. It is believed that the amount of LSO precursor affects the formation of coesite and protoenstatite. The characteristic behavior was confirmed by the differences in the LSO-LSGM Fourier map which indicates the denser electron revealed in the LSO structures in the LSO-LSGM$_B$. In this work, no reactivity of LSO-LSGM occurred on LSCF. The LSO-LSGM could be the promising SOFC electrolyte with excellent chemical stability and low impurities through an adjustment of the mass ratio between LSO and LSGM. Moreover, it can be confirmed that the mass target could be the characteristic parameter in the synthesis of LSO. The optimum composition of LSO-LSGM composite electrolyte with enhanced chemical reactivity toward LSCF cathode which was found in this study will open a new possibility for the development of SOFC component with low thermochemical reactivity during the high operating temperature of SOFC cell through a key parameter of a mass target during LSO precursor synthesis.

Acknowledgments

The authors would like to thank the Academic Leadership Grant 2023 Universitas Padjadjaran and Directorate General for Higher Education, Ministry of Ristek Dikti Republik Indonesia (No. 1549/UN6.3.1/PT.00.2023) for the financial support. The authors also thank the Department of Applied Chemistry, Tokyo Metropolitan University for allowing the author to use the XPS instrument.

References

Abdalla, A.M., Hossain, S., Azad, A.T., Petra, P.M.I., Begum, F., Eriksson, S.G., Azad, A.K., 2018. Nanomaterials for Solid Oxide Fuel Cells: A Review. *Renewable and Sustainable Energy Reviews*, Volume 82, pp. 353–368

Adi, W.A., Manaf, A., Ridwan, 2017. Absorption Characteristics of the Electromagnetic Wave and Magnetic Properties of the $La_{0.8}Ba_{0.2}Fe_xMn_{½(1-x)}Ti_{½(1-x)}O_3$ (x = 0.1–0.8) Perovskite System. *International Journal of Technology,* Volume 8(5), pp. 887–897

Baran, E.J., 1975. Infrared Spectrum of LaGaO3. *Z. Naturforsch*, Volume 30, pp. 136–137

Byszewski, P., Aleksiyko, R., Berkowski, M., Fink-finowicki, J., Diduszko, R., Gebicki, W., Baran, J., Antonova, K., 2006. IR and Raman Spectroscopy Correlation with The Structure of $(La/Pr)_{1-x}(Pr/Nd)_xGaO_3$ Solid Solution Crystals. *Journal of Molecular Structure*, Volume 793, pp. 62–67

Degen, T., Sadki, M., Bron, E., König, U., Nénert, G., 2014. The HighScore Suite. *Powder Diffraction,* Volume 29(S2), pp. S13–S18

Fan, B., Yan, J., Yan, X., 2011. The Ionic Conductivity, Thermal Expansion Behavior, and Chemical Compatibility of La0.54Sr0.44Co0.2Fe0.8O3-δ as SOFC Cathode Material. *Solid State Sciences*, Volume 13(10), pp, 1835–1839

Galindo-Hernández, F., Gómez, R., 2009. Fourier Electron Density Maps for Nanostructured TiO2 and TiO2-CeO2 Sol-Gel Solid. *Journal of Nano Research,* Volume 5, pp. 87–94

Higuchi, Y., Sugawara, M., Onishi, K., Sakamoto, M., & Nakayama, S. 2010. Oxide Ionic

Conductivities of Apatite-Type Lanthanum Silicates and Germanates and Their Possibilities as an Electrolyte of Lower Temperature Operating SOFC. *Ceramics International*, Volume 36(3), pp. 955–959

Huang, K.Q., Goodenough, J.B., 2000. A Solid Oxide Fuel Cell Based on Sr- And Mg-Doped $LaGaO_3$ Electrolyte: The Role of a Rare-Earth Oxide Buffer. *Journal of Alloys and Compounds*. Volume 303, pp. 454–464

Kalinkina, E.V, Kalinkin, A.M., Forsling, W., Makarov, V.N., 2001. Sorption of atmospheric carbon dioxide and structural changes of Ca and Mg silicate minerals during grinding. *International Journal of Mineral Processing.* Volume 61(4), pp. 289–299

Karakchiev, L.G., Avvakumov, E.G., Gusev, A.A., Vinokurova, O.B., 2009. Possibilities of Exchange Mechanochemical Reactions in the Synthesis of Magnesium Silicates. *Chemistry for Sustainable Development*, Volume 17, pp. 581–586

Kharlamova, T.S., Matveev, A.S., Ishchenko, A. V, Salanov, A.N., Koshcheev, S. V, Boronin, A.I., Sadykov, V.A., 2014. Synthesis and Physicochemical and Catalytic Properties of Apatite Type Lanthanum Silicates. *Kinetics and Catalysis*, Volume 55(3), pp. 361–362

Kharton, V.V., Marques, F.M.B., Atkinson, A., 2004. Transport Properties of Solid Oxide Electrolyte Ceramics: A Brief Review. *Solid State Ionics*, Volume 174(1–4), pp. 135–149

Kim, Y., Shin, D.-K., Shin, E.-C., Seo, H.-H., Lee, J.-S., 2011. Oxide Ion Conduction Anisotropy Deconvoluted in Polycrystalline Apatite-Type Lanthanum Silicates. *Journal of Materials Chemistry*, Volume 21, pp. 2940–2949

León-Reina, L., Losilla, E.R., Martínez-Lara, M., Bruque, S., Aranda, M.A., 2004. Interstitial Oxygen Conduction in Lanthanum Oxy-Apatite Electrolytes. *Journal of Materials Chemistry,* Volume 14(7), pp. 1142–1149

Malik, Y.T., Noviyanti, A.R., Syarif, D.G., 2018. Lowered Sintering Temperature on Synthesis of $La_{9.33}Si_6O_{26}$ (LSO) – $La_{0.8}Sr_{0.2}Ga_{0.8}Mg_{0.2}O_{2.55}$ (LSGM) Electrolyte Composite and the Electrical Performance on $La_{0.7}Ca_{0.3}MnO_3$ (LCM) Cathode. *Journal of Scientific and Applied Chemistry*, Volume 21(4), pp. 205–2010

Martinez, J.R., Vázquez-Durán, A., Martinez-Duran, G., Ortega-Zarzosa, G., Palomares-Sánchez, S.A., Ruiz, F., 2008. Coesite Formation at Ambient Pressure and Low Temperatures, *Advances in Materials Science and Engineering*, Volume 2008, p. 406067

Masson, O., Berghout, A., Béchade, E., Jouin, J., Thomas, P., Asaka, T., Fukuda, K., 2017. Local Structure and Oxide-Ion Conduction Mechanism in Apatite-Type Lanthanum Silicates. *Science and Technology of Advanced Materials*, Volume 18(1), pp. 644–653

Minh, N.Q., Takahashi, T., 1995. Cathode. *Science and Technology of Ceramic Fuel Cells*. Amsterdam: Elsevier Science B.V.

Mulyazmi, Daud, W.R.W., Rahman, E.D., Purwantika, P., Mulya, P.A., Sari, N.G., 2019. Effect of Operating Conditions on the Liquid Water Content Flowing Out of the Cathode Side and the Stability of PEM Fuel Cell Performance. *International Journal of Technology,* Volume 10(3), pp. 634–643

Noviyanti, A.R., Hastiawan, I., Eddy, D.R., Adham, M.B., Hardian, A., Syarif, D.G. 2018. Preparation and Conductivity Studies of $La_{9.33}Si_6O_{26}$ (LSO) -$CeE_{0.85}Gd_{0.15}O_{1.925}$ (CGO_{15}) Composite Based Electrolyte for IT-SOFC. *Oriental Journal of Chemistry*, Volume 34(4), pp. 2125–2130

Noviyanti, A.R., Irwansyah, F.S., Hidayat, S., Hardian, A., Syarif, D.G., Yuliyati, Y.B., Hastiawan, I., 2016. Preparation and Conductivity of Composite Apatite $La_{9.33}Si_6O_{26}$ (LSO)-$Zr_{0.85}Y_{0.15}O_{1.925}$ (YSZ). *In*: AIP Conference Proceedings, Volume 1712(1), p. 050002

Noviyanti, A.R., Juliandri, J., Winarsih, S., Syarif D.S., Malik, Y.T., Septawendar, R., Risdiana R., 2021. Highly Enhanced Electrical Properties of Lanthanum-Silicate-

Oxide-Based SOFC Electrolytes with Co-Doped Tin and Bismuth in $La_{9.33-x}Bi_xSi_{6-y}Sn_yO_{26}$. *RSC Advances***,** Volume 11**,** pp. 38589–38595

Preux, N., Rolle, A., Vannier, R.N., 2012. *Electrolytes and Ion Conductors Forfor Solid Oxide Fuel Cells (SOFCs)*. Woodhead Publishing Limited

Raghvendra, Singh, R.K., Singh, P., 2014. Electrical Conductivity of LSGM-YSZ Composite Materials Synthesized via Coprecipitation Route. *Journal of Materials Science*, Volume 49(16), pp. 5571–5578

Rahmawati, F., Permadani, I., Syarif, D., Soepriyanto, S., 2017. Electrical Properties of Various Composition of Yttrium Doped-Zirconia Prepared from Local Zircon Sand. *International Journal of Technology,* Volume 8(5), pp. 939–946

Rajesh, R., Singh, K., 2014. Electrical Conductivity of LSGM – YSZ Composite Materials Synthesized via Coprecipitation Route. *Journal of Materials Science,* Volume 49(16), pp. 5571–5578

Raza, R., Zhu, B., Ra, A., Raza, M., Lund, P., 2020. Functional Ceria-Based Nanocomposites for Advanced Low- Temperature (300-600°C) Solid Oxide Fuel Cell: A Comprehensive Review. *Materials Today Energy*, Volume 15, p. 100373

Zarkov, A., Stanulis, A., Sakaliuniene, J., Butkute, S., 2015. On The Synthesis of Yttria-Stabilized Zirconia: A Comparative Study. *Journal of Sol-Gel Science and Technology*. Volume 76(2), pp. 309–319